

Online Research @ Cardiff

This is an Open Access document downloaded from ORCA, Cardiff University's institutional repository: <https://orca.cardiff.ac.uk/id/eprint/144682/>

This is the author's version of a work that was submitted to / accepted for publication.

Citation for final published version:

Chen, Bo, Hu, Chunlin, Mills, Benjamin J. W., He, Tianchen, Andersen, Morten B. ORCID: <https://orcid.org/0000-0002-3130-9794>, Chen, Xi, Liu, Pengju, Lu, Miao, Newton, Robert J., Poulton, Simon W., Shields, Graham A. and Zhu, Maoyan 2022. A short-lived oxidation event during the early Ediacaran and delayed oxygenation of the Proterozoic ocean. *Earth and Planetary Science Letters* 577 , 117274. 10.1016/j.epsl.2021.117274 file

Publishers page: <https://doi.org/10.1016/j.epsl.2021.117274>
<<https://doi.org/10.1016/j.epsl.2021.117274>>

Please note:

Changes made as a result of publishing processes such as copy-editing, formatting and page numbers may not be reflected in this version. For the definitive version of this publication, please refer to the published source. You are advised to consult the publisher's version if you wish to cite this paper.

This version is being made available in accordance with publisher policies.

See

<http://orca.cf.ac.uk/policies.html> for usage policies. Copyright and moral rights for publications made available in ORCA are retained by the copyright holders.



1 **A short-lived oxidation event during the early Ediacaran and delayed**
2 **oxygenation of the Proterozoic ocean**

3 Bo Chen¹, Chunlin Hu^{1,2}, Benjamin J. W. Mills³, Tianchen He^{3,1}, Morten B. Andersen⁴, Xi
4 Chen⁵, Pengju Liu⁶, Miao Lu¹, Robert J. Newton³, Simon W. Poulton³, Graham A. Shields⁷,
5 Maoyan Zhu^{1,2*}
6

7 ¹State Key Laboratory of Palaeobiology and Stratigraphy & Center for Excellence in Life and
8 Paleoenvironment, Nanjing Institute of Geology and Palaeontology, Chinese Academy of
9 Sciences, Nanjing, China.

10 ²College of Earth and Planetary Sciences, University of Chinese Academy of Sciences,
11 Beijing, China.

12 ³School of Earth and Environment, University of Leeds, Leeds, LS2 9JT, UK.

13 ⁴School of Earth and Ocean Sciences, Cardiff University, Cardiff, CF10 3AT, UK.

14 ⁵State Key Laboratory for Mineral Deposits Research, School of Earth Sciences and
15 Engineering, Nanjing University, Nanjing, China.

16 ⁶MNR Key Laboratory of Stratigraphy and Palaeontology, Institute of Geology, Chinese
17 Academy of Geological Sciences, Beijing 100037, China

18 ⁷Department of Earth Sciences, University College London, Gower Street, London, WC1E 6BT,
19 UK.

20
21 *email: myzhu@nigpas.ac.cn
22

23 **The Ediacaran Period was characterised by major carbon isotope perturbations. The**
24 **most extreme of these, the ~570 Ma Shuram/DOUNCE (**Doushantuo Negative Carbon****
25 **isotope Excursion)** anomaly, coincided with early radiations of benthic macrofauna linked
26 **to a temporary expansion in the extent of oxygenated seawater. Here we document an**
27 **earlier negative excursion (the ~610 Ma WANCE (**Weng'An Negative Carbon****
28 **isotope Excursion)** anomaly in the Yangtze Gorges area, South China, that reached
29 **equally extreme carbon isotope values and was associated with a similar degree of**
30 **environmental perturbation. Specifically, new uranium isotope data evidence a significant,**

31 **but transient, shift towards more oxygenated conditions in tandem with decreasing**
32 **carbon isotope values, while strontium and sulfur isotope data support an increase in**
33 **continental weathering through the excursion. We utilize a biogeochemical modelling**
34 **approach to demonstrate that the influx of such a weathering pulse into an organically-**
35 **laden, largely anoxic ocean, fully reproduces each of these distinct isotopic trends. Our**
36 **study directly supports the hypothesis that a large dissolved marine organic pool**
37 **effectively buffered against widespread oxygenation of the marine environment through**
38 **the Proterozoic Eon, and in doing so, substantially delayed the radiation of complex**
39 **aerobic life on Earth.**

40

41 **Key words: DOM (Dissolved Organic Matter), carbon isotope perturbations, strontium**
42 **isotopes, sulfur isotopes, uranium isotopes, Metazoans**

43

44 **1. Introduction**

45 The Ediacaran-Cambrian transition was characterised by high amplitude $\delta^{13}\text{C}$ excursions in
46 seawater (e.g. the ‘Shuram/DOUNCE’ isotope excursion), with negative values far below
47 mantle input ($\sim -6\%$, V-PDB) (Burns and Matter, 1993; Grotzinger et al., 2011; Zhu et al., 2013;
48 Shields et al., 2019). These extreme $\delta^{13}\text{C}$ anomalies are difficult to interpret using conventional
49 carbon isotope mass balance, as they imply net consumption of oxygen by the carbon cycle
50 (Lee et al., 2015), causing some to argue for a diagenetic or regional origin for these signals
51 (Knauth and Kennedy 2009). It is, however, increasingly evident that Ediacaran-age negative
52 $\delta^{13}\text{C}$ excursions are identical and correlative on a global scale (Xiao et al., 2016), reflecting a
53 well-mixed primary seawater signal (Grotzinger et al., 2011; Lu et al., 2013).

54 Alternatively, it has been proposed that episodic oxidation of a large deep marine dissolved
55 organic matter (DOM) reservoir released surplus ^{13}C -depleted carbon (around -30% , V-PDB)

56 into the ambient dissolved inorganic carbon (DIC) reservoir at times during the Ediacaran
57 Period, resulting in the observed highly-negative $\delta^{13}\text{C}$ anomalies (Rothman et al., 2003).
58 However, this sequence of events has been questioned due to an apparent insufficient supply of
59 oxidant (e.g. O_2 , SO_4) to the Ediacaran ocean to sustain DOM oxidation over the multimillion-
60 year timescales required (Bristow and Kennedy, 2008). Recently, however, Shields et al. (2019)
61 used a biogeochemical model to show that a pulse of sulfate into the ocean from rapid
62 continental gypsum dissolution could have supplied sufficient oxidizing capacity to produce
63 the carbon isotope change evident in the ~570 Ma Shuram/DOUNCE event.

64 While this recent work has resolved the theoretical challenge to the DOM buffer hypothesis,
65 direct geochemical evidence supporting this proposed chain of events is lacking, which is also
66 the case with other super-negative carbon isotope excursions during the Neoproterozoic Era.
67 Here, we present an integrated carbon, sulfur, uranium and strontium isotope study of the ~610
68 Ma WANCE anomaly in the Yangtze Gorges area, South China that provides the first direct
69 geochemical evidence supporting the DOM buffer hypothesis. We then utilize the COPSE
70 (Carbon, Oxygen, Phosphorus, Sulphur and Evolution) biogeochemical model to reproduce
71 each of these distinct isotopic trends by setting up forcing parameters in line with the DOM
72 buffer hypothesis. The robustness and universal implication of the DOM effect is further tested
73 by investigating longer time-scale records for the Ediacaran and early Cambrian.

74

75 **2. Geological setting and stratigraphy**

76 Ediacaran strata, deposited in various settings ranging from shallow marine shelf to deep
77 marine basin (Zhu et al., 2007) (Fig. 1), are well exposed over the Yangtze Platform of South
78 China. The Yangtze Gorges area in western Hubei Province contains the most classic
79 succession, comprising the Doushantuo Formation and overlying Dengying Formation, and has
80 been intensively investigated over the past century (Zhu et al., 2007, 2013; Zhou et al., 2018)

81 (Fig. 1a, b, c). The Doushantuo Formation in the Yangtze Gorges area mainly comprises
82 limestone with alternating organic-rich black shale and/or thinly bedded dolostone and
83 phosphorite-chert nodules that were deposited in an offshore intra-shelf basin within the
84 Yangtze platform (Zhu et al., 2013). Traditionally, the Doushantuo Formation is subdivided
85 into four members (Members I–IV) based on their distinct lithologic characteristics in the
86 Yangtze Gorges area (Zhou et al., 2018). Three major negative C-isotopic excursions known as
87 EN1, (Ediacaran negative $\delta^{13}\text{C}$ excursion 1), (EN2, Ediacaran negative $\delta^{13}\text{C}$ excursion 2) and
88 (EN3, Ediacaran negative $\delta^{13}\text{C}$ excursion 3) were previously identified within the Doushantuo
89 Formation and are widely used as key chemostratigraphic markers for both regional and global
90 stratigraphic correlations (Zhou et al., 2018; McFadden et al., 2008). However, subsequent
91 higher-resolution investigations found an additional $\delta^{13}\text{C}$ negative anomaly between EN1 and
92 EN2 that is associated with a sequence boundary in the middle Doushantuo Formation
93 deposited in the shallow shelf area of the Yangtze platform (Zhu et al., 2013; Gao et al., 2018,
94 Fig. 2), indicating that there are at least four distinct negative carbon isotope excursions within
95 the Doushantuo Formation, which, in ascending order, are named CANCE (CAP carbonate
96 Negative Carbon isotope Excursion) (EN1), WANCE, BAINCE (Baiguoyuan Negative Carbon
97 isotope Excursion (EN2) and DOUNCE (EN3) according to Zhou et al. (2018) and Zhu et al.
98 (2013) (Fig 1c; Fig. 2).

99 The Nantuocun section is located along a roadcut above the southern bank of the Yangtze
100 River ca. 3 km east of Sanduping town, at a site exactly opposite the well-known Liantuo Bridge
101 on the northern bank of the Yangtze River. At this locality, the Doushantuo Formation outcrops
102 as a basal cap carbonate (Member I) with overlying black shales followed by a ca. 40 meter-
103 thick carbonate succession (lower part of Member II) dominated by dolostone and argillaceous
104 dolostone with chert nodules (Fig. 1d; Fig. S1). Abundant acritarch fossils were recovered in
105 the chert nodules, including *Tianzhushania spinosa*, *Appendisphaera grandis*, *Estrella greyae*,

106 *Estrella recta*, *Estrella sp.*, *Dicrospinasphaera improcera*, *Distosphaera speciose*,
107 *Ericiasphaera magna*, *Membranosphaera Formosa* and *Mengeosphaera lunula*.
108 Biostratigraphic correlation of the acritarch assemblage confirms that the study interval of the
109 Nantuocun section can readily be assigned to Member II of the Doushantuo Formation (Liu and
110 Moczyłowska, 2019) (Fig. 1d), in line with independent correlation by means of litho- and
111 carbon isotope stratigraphy (Fig. 1d). Based on the integrated correlation above, the extreme
112 negative $\delta^{13}\text{C}_{\text{carb}}$ excursion observed in the Nantuocun section cannot be assigned to the
113 DOUNCE anomaly, which is known from members 3 and 4 of the Doushantuo Formation only,
114 and so is proposed to be time equivalent to the WANCE event reported from the middle part of
115 Member II that was dated to 609 ± 5 Ma by the zircon SIMS U-Pb method (Zhou et al., 2017).
116 The lower and upper boundaries of the Doushantuo Formation in the Yangtze Gorges area are
117 well constrained to ca. 635 Ma and ca. 551 Ma, respectively, by high precision U-Pb zircon
118 ages (Condon et al., 2005). However, high-precision radiometric ages are rare within the
119 formation, hampering the subdivision and global correlation of Doushantuo strata as well as
120 precise constraints on the extreme carbon cycle perturbations observed in this formation.
121 However, cyclostratigraphy has been increasingly utilized to constrain the timing and duration
122 of Ediacaran geochemical and/or extreme climatic events (Sui et al., 2018). For examples, Sui
123 et al. (2018) identified 27 long-eccentricity (405 kyr) cycles from ca. 22.3 m strata in the lower
124 Doushantuo Formation at the Jiulongwan section of the Yangtze Gorges area about 7 km from
125 the Nantuocun section, suggesting an average sediment accumulation rate (SAR) of 1.95 m/Ma
126 for the Doushantuo Members II. Based on this suggestion, the three meters of strata that record
127 the WANCE event observed at Nantuocun section are estimated to have accumulated within
128 about 1.5 Myr.

129

130 **3. Methods**

131 **3.1 Carbonate carbon and oxygen isotopes**

132 Carbonate powders were drilled from freshly cut rock slab surfaces using a micro-drill for
133 carbon and oxygen isotope analyses. Fine-grained micrites were preferentially selected.
134 Powders were reacted with 100% phosphoric acid at 70°C and analyzed for carbon and oxygen
135 isotopes using a Kiel IV device connected to a Finnigan MAT 253 mass spectrometer at the
136 Nanjing Institute of Geology and Palaeontology. Reproducibility was better than $\pm 0.03\%$ and
137 $\pm 0.08\%$ (1s.d.) for carbon and oxygen isotopes, respectively. All analyses were calibrated to
138 the Chinese National Standard (GBW-04405), an Ordovician carbonate from a site near Beijing,
139 with a $\delta^{13}\text{C}$ value of 0.57% and $\delta^{18}\text{O}$ value of -8.49% . All data are given in per mil (‰) relative
140 to V-PDB.

141

142 **3.2 Organic carbon isotopes**

143 For organic carbon isotope analyses, about 5 g of powdered carbonate was reacted with
144 concentrated HCl, followed by repeat checks using drops of HCl to confirm complete
145 decarbonization. The residues were then repeatedly washed with deionized water until the pH
146 reached near neutral, and samples were dried in an oven. The residues were then wrapped into
147 tin capsules for organic carbon isotope and total organic carbon (TOC) measurements, which
148 were performed with a Flash EA 2000 elemental analyser connected online to a Thermo
149 Finnigan Delta V Plus mass spectrometer. All carbon isotope values are reported in the
150 conventional δ -notation in permil relative to V-PDB. Reproducibility of the analyses was
151 checked by replicate analyses of laboratory standards black carbon (GBW04407) and Urea
152 (IVA33802174). Reproducibility was better than 0.2% for $^{13}\text{C}_{\text{org}}$, and $0.02 \text{ wt}\%$ for TOC.

153

154 **3.3 Carbonate-associated sulfate (CAS) and pyrite sulfur isotopes**

155 This study used a state-of-the-art CAS extraction method (He et al., 2020) and extraction work
156 was carried out in the Cohen Geochemistry laboratory, University of Leeds. For bulk carbonate
157 samples, 8-10 g of fine powder was first bleached in 6% NaOCl for 48 hours to remove oxidize
158 organic sulfur and metastable sulfide minerals, followed by a five times wash in 10% NaCl
159 solution for 24 hours to remove the non-CAS sulfur-bearing compounds or easily soluble
160 sulfate. Pre-bleached carbonate residues were then treated with 6 M HCl to extract CAS. CAS
161 was collected by precipitation as barium sulfate. We also measured sulfur concentrations in the
162 extracted solution using a Thermo Fisher iCAP 7400 Radial Inductively Coupled Plasma
163 Optical Emission 280 Spectrometer (ICP-OES) in the Cohen Geochemistry laboratory,
164 University of Leeds. Pyrite extractions were performed following an HCl digestion and
165 chromous chloride distillation method (Canfield et al., 1986). The barium sulfate precipitates
166 from the CAS extraction and silver sulfide from the pyrite extraction were weighed into tin
167 cups, which were combusted to yield SO₂. $\delta^{34}\text{S}$ values were determined using a Flash EA 2000
168 elemental analyzer coupled to a Delta-Advantage mass spectrometer at the NIGPAS. All
169 samples and standards are reported relative to the Vienna Canon Diablo Troilite (V-CDT)
170 standard, with an analytical reproducibility of 0.3‰ calculated from replicate analyses of IAEA
171 standards (NBS-127, IAEA-1, IAEA-SO-6).

172

173 **3.4 Elemental concentrations**

174 Approximate 50 mg of sample powder was weighed and dissolved in 3 mL of distilled 1 M
175 acetic acid and left to dissolve overnight. The solutions were centrifuged, and the supernatant
176 transferred to another breaker. The residues were rinsed three times using ultrapure water and
177 the solutions were added to the previous supernatant. The leachates were converted to nitric
178 acid medium, which was then used for elemental analysis. Element analysis was carried out at
179 the element laboratory in the NIGPAS. Trace and REE concentrations were determined using

180 an Agilent 7700A inductively coupled plasma mass spectrometer (ICP-MS) with analytical
181 precision better than $\pm 2\%$. Major elements were measured using an Agilent 710 ICP-OES with
182 analytical precision better than $\pm 5\%$.

183

184 **3.5 Strontium isotopes**

185 The samples having lower Mn/Sr ratios (< 2) were selected for strontium isotope analyses. The
186 carbonate powders were mixed with 0.5 N acetic acid, and the solution was then centrifuged at
187 3300 rpm for 10 min, after which the supernatant was dried down on a hotplate and redissolved
188 in 1.5 ml of 1.5 N HCl before ion exchange purification. A Biorad AG50W-X8 cation exchange
189 column was used to separate Sr from other elements. The diluted solutions (50 ppb Sr) were
190 introduced into a Nu Instruments *Nu Plasma II* MC-ICP-MS (Wrexham, Wales, UK) through
191 a Teledyne Cetac Technologies *Aridus II* desolvating nebulizer system (Omaha, Nebraska,
192 USA) for $^{87}\text{Sr}/^{86}\text{Sr}$ analysis. Raw data for Sr isotopic ratios were internally corrected for mass
193 fractionation by normalizing to $^{86}\text{Sr}/^{88}\text{Sr} = 0.1194$ with exponential law. International isotopic
194 standards NIST SRM 987 were periodically analyzed to correct instrumental drift. Standard
195 sample NBS 987 was measured every three samples, yielding an average value of 0.710240 ($\sigma =$
196 ± 0.000045 , $n=17$). The standard error for Sr isotope analysis was between 0.000004-0.000008,
197 All results were corrected to NIST 987 as 0.710248. Sr isotope measurements were carried out
198 at Nanjing FocuMS Technology Co. Ltd.

199

200 **3.6 Uranium isotopes**

201 For carbonate-associated uranium isotopes ($^{238}\text{U}/^{235}\text{U}$ reported as $\delta^{238}\text{U}_{\text{CAU}}$) analysis, between
202 0.2 to 1 g of carbonate powder was digested using excess 1 N HCl at room temperature for
203 several hours, until no further effervescence was observed. The leachate was separated from
204 any residue and spiked with the IRMM3636 ^{236}U - ^{233}U double spike. Uranium purification was

205 performed using a double-stage TRU and U-Teva column chemistry (Andersen et al., 2015).
206 Full uranium recovery (>95%) and practically matrix-free samples were obtained with this
207 method, with total procedural U chemistry blank <20 pg. The analyses were carried out on a
208 Nu Instruments *Nu Plasma II* MC-ICP-MS (Wrexham, Wales, UK) through Teledyne Cetac
209 Technologies *Aridus II* desolvating nebulizer system (Omaha, Nebraska, USA) at CELTIC,
210 Cardiff University. The U isotope measurements were conducted in 0.3 N HNO₃ + 0.02 N HF
211 at low mass resolution (M/M ~400). The data were collected in static mode for all the isotopes
212 of interest (²³²Th, ²³³U, ²³⁴U, ²³⁵U, ²³⁶U, ²³⁸U) in Faraday cups fitted with 11¹¹ Ω resistors,
213 generally following the set-up in Stirling et al. (2007). General U transmission efficiencies were
214 ~1% and measurements were conducted using typical ²³⁸U ion beams of ~4 x 10⁻¹⁰ amps with
215 data integration over a 60 x 5 seconds period. Washout in between samples consisted of a
216 sequence of ~3 min 0.3 N HNO₃, ~3 min 0.3 N HNO₃-0.01 N HF, and ~2 min of 0.3 N HNO₃.
217 The final wash also served as an on-peak blank measurement and was subtracted from the
218 succeeding sample measurement. Corrections of ²³⁸U and ²³⁵U impurities in IRMM3636, tailing,
219 H⁺ formation and mass bias corrections followed Andersen et al. (2014, 2015, 2016). The
220 accuracy of the set-up was first tested by measuring secondary standards bracketed and
221 normalized to the CRM 145 standard spiked, and measured in a similar manner to the unknowns.
222 The ²³⁸U/²³⁵U ratios are reported as $\delta^{238}\text{U} (= 1.000 \times [(^{238}\text{U}/^{235}\text{U})_{\text{Sample}} / (^{238}\text{U}/^{235}\text{U})_{\text{CRM-145}} -$
223 1]). Values are reported relative to the NBL CRM-145 natural U standard. The internal
224 precision on measured $\delta^{238}\text{U}$ values are better than $\pm 0.05\%$ (2 standard error) for all samples.
225 The external reproducibility of $\delta^{238}\text{U}$ for the in-house CZ-1 gave $\delta^{238}\text{U}$ of $-0.04 \pm 0.07\%$ (2 sd,
226 11 measurements) in good agreement with previously reported values (e.g. Andersen et al.,
227 2014, 2015, 2016; Stirling et al., 2007), while duplicate measurements of HU-1 (-0.56 ± 0.06
228 and -0.58 ± 0.05 , 2 standard error) are also in very good agreement with previously reported
229 results (Hiess et al., 2012).

230

231 **4. Results**

232 We present strontium, uranium and sulfur isotope analyses through a newly identified negative
233 $\delta^{13}\text{C}_{\text{carb}}$ excursion, which exhibits a sharp fall from +6‰ to a nadir of -10‰, followed by a
234 sharp recovery within an ~3 meter interval of the lower Doushantuo Formation (early Ediacaran)
235 in the Yangtze Gorges area, South China (Fig. 3, Fig. S2). Integrated stratigraphic data suggest
236 that the negative $\delta^{13}\text{C}_{\text{carb}}$ excursion is correlative to the WANCE excursion and therefore
237 predates the well-known ‘Shuram/DOUNCE’ event by about 30 Myr (see Fig. 1 and 2).

238 An evaluation of possible diagenetic alteration of carbon, strontium, uranium and sulfur
239 isotope data based on geochemical crossplots, petrographic and mineralogical observations, and
240 regional stratigraphic correlations suggests that this event archives a primary seawater
241 geochemical perturbation that was widespread (see more details in the Supplementary
242 Information), at least extending across the Yangtze Gorges area in South China (Fig. 2)

243 $\delta^{34}\text{S}_{\text{CAS}}$ values from the Nantuocun section show a significant increase from +40‰ to +60‰
244 beneath the WANCE followed by a sharp decline to +30‰ (V-CDT) alongside the falling limb
245 of the WANCE (Fig. 3), accompanied by ~10‰ (V-CDT) decrease in pyrite sulfur isotope
246 values ($\delta^{34}\text{S}_{\text{pyr}}$) (Fig. 3). Both $\delta^{34}\text{S}_{\text{CAS}}$ and $\delta^{34}\text{S}_{\text{pyr}}$ values are relatively invariant above the
247 WANCE. The $\delta^{238}\text{U}$ values show relatively stable values around -0.55 ‰ below the WANCE
248 followed by a sharp rise to -0.2‰, parallel with the falling limb of the WANCE, an abrupt
249 decrease to -0.86‰ as $\delta^{13}\text{C}$ values reach their nadir, and then by relatively invariant values
250 around -0.55‰. Strontium isotope ($^{87}\text{Sr}/^{86}\text{Sr}$) data from the section reveal a pronounced
251 increase from ~0.7078 to ~0.7084, succeeded by a decrease to ~0.7081, following which there
252 was no significant change. The $^{87}\text{Sr}/^{86}\text{Sr}$ increase initiated prior to the WANCE, whereas the
253 decline coincides with the nadir of $\delta^{13}\text{C}_{\text{carb}}$ (Fig. 3).

254

255 **5. Discussion**

256 **5.1 A short-lived oxidation event during the early Ediacaran**

257 As shown in Figure 4, seawater sulfate ($\delta^{34}\text{S}_{\text{CAS}}$) and pyrite ($\delta^{34}\text{S}_{\text{pyr}}$) sulfur isotope values
258 fell by $\sim 30\text{‰}$ and $\sim 10\text{‰}$ (V-CDT), respectively, alongside the falling limb of the $\delta^{13}\text{C}_{\text{carb}}$
259 excursion. As in the later Shuram excursion, the substantial long-term decrease in $\delta^{34}\text{S}$ may
260 indicate a large pulse of sulfate input into a sulfate-poor ocean (Shi et al., 2018), effectively
261 resetting the isotope composition closer to that of the weathered gypsum (and pyrite), which
262 was likely no higher than $+15\text{‰}$ (Shields et al., 2019). The extreme-negative $\delta^{13}\text{C}$ excursion is
263 consistent with oxidation of DOM, and the presence of a brief oxygenation event is further
264 supported by evidence from carbonate-associated uranium isotope values, which are utilized as
265 a proxy for oceanic $\delta^{238}\text{U}$. This record exhibits an abrupt rise in $\delta^{238}\text{U}_{\text{CAU}}$ just before the nadir
266 in the C isotope record, from initial values below, to values above, modern oxygenated seawater
267 ($\sim -0.4\text{‰}$) (Fig. 3). Rising $\delta^{238}\text{U}_{\text{CAU}}$ values are associated with reduced rates of sequestration of
268 isotopically heavy uranium under anoxic conditions globally, which increases $\delta^{238}\text{U}$ in the
269 ocean (Andersen et al., 2014). Thus, the increasing $\delta^{238}\text{U}_{\text{CAU}}$ trend associated with WANCE
270 likely documents a rapid expansion of oxic seafloor area in the early Ediacaran ocean.

271 The onset of the WANCE event is also marked by an increase in seawater $^{87}\text{Sr}/^{86}\text{Sr}$, alongside
272 a rise in $\delta^{34}\text{S}_{\text{CAS}}$ towards its highest value in the geological record ($\sim 60\text{‰}$) (Fike et al., 2015)
273 (Fig. 3). The combination of rising seawater $^{87}\text{Sr}/^{86}\text{Sr}$ and sulfate $\delta^{34}\text{S}$, alongside much lower
274 pyrite $\delta^{34}\text{S}$, suggests that enhanced weathering, likely due to tectonic uplift associated with the
275 amalgamation of Gondwana (Campbell and Squire, 2010), may have exhumed major basin-
276 scale evaporite previously deposited during the Tonian Period (Turner and Bekker, 2016) or
277 earlier, resulting in high pyrite burial rates. This is because a large isotopic fractionation
278 between sulfate and pyrite ($\Delta\delta_{\text{CAS-pyr}} > \sim 35\text{‰}$) (Fig. 3) is only compatible with abundant
279 dissolved sulfate (Habicht and Canfield, 2018), while pyrite burial is related through organic

280 production to weathering input of nutrients as well as sulfate. By contrast, the sharp drop in
281 $\Delta\delta_{\text{CAS-pyr}}$ to significantly lower values ($\sim 20\%$) around the lowest point of the negative $\delta^{13}\text{C}_{\text{carb}}$
282 excursion, may signal a return to lower oceanic sulfate concentrations and reduced rates of
283 pyrite burial, alongside greater oxidation of continental pyrite (Fig.3).

284

285 **5.2 Reproducing the oxidation event in the COPSE biogeochemical model**

286 Our combined carbon, sulfate, strontium and uranium isotope data suggest that the
287 WANCE represents a marine oxygenation event driven by enhanced weathering input of sulfate,
288 with the extent of oxygenation mediated by oxidation of a large marine DOM reservoir. In order
289 to quantitatively test this hypothesis, we employ the COPSE biogeochemical model (Bergman
290 et al., 2004), which computes the major long-term fluxes of carbon, oxygen, phosphorus,
291 nitrogen and sulfur through Earth's hydrosphere and crust. COPSE is a 'forwards' model in
292 which processes are driven by a set of evolving boundary conditions (forcing factors) and
293 internal dynamics, including a nutrient-driven biosphere (See Supplementary Information for
294 full model description). We use the latest COPSE model revision (Tostevin and Mills, 2020)
295 which includes forcing information for the Ediacaran Period (Williams et al., 2019) and
296 simplified DOM reservoir dynamics (Shields et al., 2019). See bjwmills.com for model code.

297

298 We run COPSE through the Ediacaran Period and impose a sulfate input event at the
299 time of the observed negative carbon isotope excursion to examine the dynamics of an
300 oxygenation event at this time. In order to make the model most applicable to the short time
301 interval being tested we make the following alterations:

- 302 1. COPSE has very strong negative feedbacks on marine sulfate concentrations and is unable
303 to reproduce the low sulfate ocean expected for the Ediacaran. To begin with low sulfate
304 concentration, we increase the power of the sulfate sinks by factor $PYR_{mod} = GYP_{mod} =$

305 10. This allows the model to enter the Ediacaran Period with $[\text{SO}_4] \approx 1 \text{ mM}$.

306 2. To match the background pre-event carbon and sulfur isotope records we set the isotopic
307 compositions of inputs from carbonates, organic carbon, pyrite and gypsum to be 5‰, -
308 20‰, 5‰ and 50‰, respectively. This is based on the observed composition of seawater
309 before the event. Similarly to match the strontium isotope record we set the Rb/Sr ratio of
310 felsic lithologies in the model to 0.29 (from 0.26 in the original model).

311

312 To drive the oxygenation event in the model we impose an input of sulfate from the
313 weathering of continental evaporites and pyrites at 610.5 Ma, coinciding with the beginning of
314 the strontium and carbon isotope excursions. Specifically, the model forcing is:

$$315 \text{GYP}_{input} = [-1000 - 610.5 - 610.4 - 609.5 - 609.4 \ 0], [0 \ 0 \ \text{GYP}_{ramp} \ \text{GYP}_{ramp} \ 0 \ 0]$$

$$316 \text{PYR}_{input} = [-1000 - 610.5 - 610.4 \ 0], [0 \ 0 \ \text{PYR}_{ramp} \ \text{PYR}_{ramp}]$$

317 where the first vector is time in millions of years before present, and the second is the
318 additional weathering flux. We take $\text{PYR}_{ramp} = 1$ (which corresponds to a doubling) and
319 $\text{GYP}_{ramp} = 5 - 15$. It is assumed that an uplift-weathering event will result in rapid dissolution
320 of gypsum (Shields et al., 2019), whereas weathering of pyrite will be sustained at lower levels
321 over a longer period since it is a sink for O_2 . The magnitude of the weathering rate increase is
322 consistent with previous estimates for global evaporite dissolution (Shields et al., 2019;
323 Wortmann and Paytan, 2012), and requires a total gypsum supply of around $1-2 \times 10^{19} \text{ mol S}$,
324 which is well within plausible bounds. These additional inputs of sulfur are assumed to be
325 buried almost completely as pyrite (following Shields et al., 2019), although we raise the pyrite
326 burial fraction to 95% (from 80% in that paper) in order to explore the ability of the model to
327 match the extreme positive $\delta^{34}\text{S}$ values.

328

329 Our model seawater isotope ratio results are shown in Figure 4, and are compared directly
330 to our strontium, sulfur and carbon isotope data. The COPSE model does not include a uranium
331 reservoir and cannot accurately predict the behaviour of this elemental cycle because it has a
332 single ‘atmosphere-ocean’ reservoir for oxygen, with no explicit treatment of marine versus
333 atmospheric oxygenation. Instead, marine anoxia in COPSE is represented by a variable called
334 *anox*, which represents the balance between atmosphere/ocean O₂ availability and the size of
335 the marine phosphorus reservoir (i.e. O₂ is supplied to the ocean by the atmosphere and is
336 utilized during remineralization). DOM oxidation is assumed to begin once *anox* crosses a
337 certain threshold (Shields et al., 2019). In order to examine O₂ production in the model relative
338 to the marine $\delta^{238}\text{U}$ record, we qualitatively compare the U isotope data to variations in the
339 model atmosphere-ocean O₂ reservoir (Fig. 5), accepting that changes in $\delta^{238}\text{U}$ might occur
340 much more rapidly than changes to the overall surface O₂ reservoir, due to oxygen-nutrient
341 feedbacks and changes to the area of oxic seafloor (e.g. Alcott et al., 2019).

342

343 In our model scenario, the rapid increase in sulfate input from gypsum weathering leads to
344 increased rates of microbial sulfate reduction and pyrite burial, resulting in a steady rise in O₂
345 availability (Fig. 5). After around 300 kyrs, the marine anoxia threshold is crossed (when O₂
346 supply from the atmosphere is sufficient; O₂ $\approx 1 \times 10^{19}$ mol) and the DOM reservoir starts to
347 be remineralised. This drives the $\delta^{13}\text{C}$ composition of marine DIC to very low levels (Fig. 4),
348 while also placing a break on further oxygenation. Overall atmosphere-ocean O₂ content
349 continues to rise at a reduced rate (Fig. 5) until the sulfate input abates and the system quickly
350 returns to the background state. Here, O₂ is quickly consumed by the DOM reservoir until the
351 assumed anoxia threshold in the model is crossed again, after which DOM oxidation ceases and
352 $\delta^{13}\text{C}$ returns to the initial value. Figures 4 and 5 confirm that the timescale and magnitude of
353 the perturbation and recovery of carbonate $\delta^{13}\text{C}$ and $\delta^{238}\text{U}$ values are consistent with a sulfate

354 input event under a DOM buffer. One aspect we cannot investigate with the COPSE model is
355 the relatively constant $\delta^{13}\text{C}_{\text{org}}$ composition across the WANCE. This ‘decoupled’ behavior of
356 the organic and inorganic carbon pools has been linked to the presence of a large DOM reservoir
357 before (Rothman et al., 2003), but COPSE cannot recreate it because organic matter is not
358 considered as a dynamic reservoir, and sedimentary C_{org} can only be buried directly from the
359 DIC pool.

360

361 In addition to the carbon-oxygen systematics, the model also produces a reasonable fit to
362 strontium and sulfur isotope values across the WANCE event (Fig. 4). Strontium $^{87}\text{Sr}/^{86}\text{Sr}$ ratios
363 rise during the gypsum dissolution event in the model because the rapid remineralization of
364 DOM increases atmospheric CO_2 and global temperature, thus delivering more radiogenic Sr
365 to the ocean. Sr ratios in the model then level off when the weathering event abates, although
366 not to the same degree shown by the data. The measured sulfur isotope ratios show the most
367 complex pattern over this event, rising initially but then falling dramatically around the time of
368 the C isotope reversal (Fig. 4). This behaviour is replicated to some degree by the model. Here,
369 the initial rise in $\delta^{34}\text{S}$ is driven by exceptionally high pyrite burial rates as sulfate is delivered
370 to productive margins underlain by dominantly anoxic waters and sediments. When the sulfate
371 supply shuts down, the $\delta^{34}\text{S}$ ratio of seawater is reduced as pyrite burial is curtailed, and dips
372 below the pre-event value due to the low $\delta^{34}\text{S}$ values of the evaporite sulfur influx (15 ‰).

373

374 Although there are some discrepancies between the model and our dataset, these are relatively
375 minor and the overall level of qualitative and quantitative agreement over four distinct
376 geochemical proxies is strong. We therefore conclude that there was a substantial influx of
377 oxidant to the atmosphere and oceans during the WANCE, but that marine oxygenation was
378 ultimately prevented by a large reservoir of DOM. The total consumption of DOM in this case

379 is $1-2 \times 10^{19}$ mols of carbon, requiring an equal amount of molecular oxygen, equivalent to
380 around half of the present-day atmosphere-ocean reservoir.

381

382 **5.3 Delayed oxygenation of the Proterozoic ocean and implications for the rise of** 383 **metazoans**

384 Similar extreme carbon cycle perturbations are observed in later Ediacaran times, most
385 notably, the ‘Shuram/DOUNCE’ of the middle Ediacaran (eg. Lu et al., 2013). The Shuram
386 event is thought to have been a longer oxygenation event that coupled enhanced evaporite
387 weathering and DOM oxidation (Shi et al., 2018; Fike et al., 2006; McFadden et al., 2008),
388 suggesting that episodic pulsed oxidant (sulfate) input was a uniform driver behind these
389 extreme negative carbon isotope excursions of the Ediacaran Period. These, in turn, governed
390 the redox status of the Ediacaran ocean, as exemplified by dramatic oscillations comprising
391 multiple transient oxygenation events punctuated by intervals of more widespread marine
392 anoxia (Sahoo et al., 2012) (Fig. 6), while brief oxygenation during the WANCE event
393 represents an earlier excursion to a more oxygenated state.

394 Significantly, the episodic expansion of oxygenated seafloor area through the Ediacaran
395 Period may have provided variable habitable space and ecological niches for the development
396 of complex macro-eukaryotes and primitive metazoans (e.g. the Weng’an and Lantian biotas in
397 the lower Doushantuo Formation (Xiao et al., 1998; Yuan et al., 2011; Yin et al., 2015),
398 However, biological innovations in connection with these brief oxygenation events may have
399 been discrete and interrupted by evolutionary lags or extinctions due to episodic reversals back
400 to widespread marine anoxia (Zhu et al., 2013; Wood et al., 2019). Innovations requiring higher
401 oxygen demand (e.g. motility, biomineralisation, predation; Fig. 6) appear to have emerged
402 only after the mid-late Ediacaran, with diversification during the early Cambrian radiations
403 (Wood et al., 2019). These opportunistic radiations of aerobic life forms may have promoted
404 subsequent innovations and feedbacks that eventually prevented a return to the prior turbid state

405 (Butterfield et al., 2009; Lenton et al., 2014), enabling ocean oxygenation to reach near modern
406 levels by the early Cambrian (Chen et al., 2015).

407

408 **6. Conclusions**

409 Integrated carbon, sulfur, uranium and strontium isotope analyses of the ~610 Ma WANCE
410 anomaly in the Yangtze Gorges area, South China, document a brief shift towards more
411 oxygenated conditions. This oxygenation is consistent with surplus oxidant (SO₄) supply from
412 increased continental weathering that resulted in a sharp decline in carbonate δ¹³C to far below
413 mantle values (nadir ~-10‰). Once the available oxidant was exhausted, the ocean rapidly
414 returned to anoxia, accompanied by a δ¹³C recovery to positive values. This pattern is consistent
415 with observations from the ~570 Ma Shuram/DOUNCE anomaly, suggesting that surplus
416 oxidant input may have been a uniform driver behind the extreme negative carbon isotope
417 excursions of the Ediacaran Period.

418

419 The dynamic balance between ocean redox state and oxidant supply strongly supports the
420 hypothesis that a marine DOM pool effectively suppressed oxygenation of the marine
421 environment throughout most of the Proterozoic, placing a major constraint on the persistence
422 of Proterozoic ocean anoxia. Significantly, this brief oxygenation event may signal the onset of
423 a new transitional phase characterized by the pulsed destruction of a large oceanic dissolved
424 organic carbon reservoir, which ultimately facilitated the higher marine oxygen concentrations
425 required by more complex ecosystems.

426

427

428 **References**

429 Alcott, L.J., Mills, B.J.W., Poulton, S.W., 2019. Stepwise Earth oxygenation is an inherent property of global
430 biogeochemical cycling. *Science* 366, 1333-1337.

431 Andersen, M.B., Romaniello, S., Vance, D., Little, S.H., Herdman, R., Lyons, T.W., 2014. A modern
432 framework for the interpretation of $^{238}\text{U}/^{235}\text{U}$ in studies of ancient ocean redox. *Earth and Planetary*
433 *Science Letters* 400, 184-194.

434 Andersen, M. B., Elliott, T., Freymuth, H., Sims, W. W. K., Niu Y., Kelley K. A., 2015. The terrestrial
435 uranium isotope cycle. *Nature* 517, 356-359.

436 Andersen, M. B., Vance, D., Morford, J.L., Bura-Nakića, E., Breitenbach, S. F. M., Och, L., 2016. Closing
437 in on the marine $^{238}\text{U}/^{235}\text{U}$ budget. *Chemical Geology* 420, 11-22.

438 Andersen, M. B., Stirling C. H., Weyer S., 2017. Uranium Isotope Fractionation. *Reviews in Mineralogy and*
439 *Geochemistry* 82, 799-850.

440 Burns, S. J. and Matter, A., 1993. Carbon isotopic record of the latest Proterozoic from Oman. *Eclogae*
441 *Geologicae Helveticae* 86, 595–607.

442 Berner, R. A., 1991. A model for atmospheric CO_2 over Phanerozoic time. *American Journal of Science* 291,
443 339-376,

444 Bergman, N. M., Lenton, T. M. & Watson, A. J., 2004. COPSE: A new model of biogeochemical cycling
445 over Phanerozoic time. *American Journal of Science* 304, 397-437.

446 Bristow, T.F., Kennedy, M. J., 2008. Carbon isotope excursions and the oxidant budget of the Ediacaran
447 atmosphere and ocean. *Geology* 36, 863.

448 Butterfield, N. J., 2009. Oxygen, animals and oceanic ventilation: an alternative view. *Geobiology* 7, 1–7.

449 Campbell, I.H and Squire R.J. 2010. The mountains that triggered the late neoproterozoic increase in oxygen:
450 the second great oxidation event. *Geochimica et Cosmochimica Acta*, 74, 4187-4206.

451 Canfield, D. E., Raiswell, R., Westrich J. T., Reaves, C. M., Berner R. A., 1986. The use of chromium
452 reduction in the analysis of reduced inorganic sulfur in sediments and shales. *Chemical geology* 54, 149-
453 155.

454 Chen, X., Ling, H.F., Vance, D., Shields-Zhou, G.A., Zhu, M., Poulton, S.W., Och, L.M., Jiang, S.Y., Li, D.,
455 Cremonese, L., Archer, C., 2015. Rise to modern levels of ocean oxygenation coincided with the
456 Cambrian radiation of animals. *Nature Communications*. 6, 7142.

457 Condon, D., Zhu, M., Bowring, S., Wang, W., Yang, A., Jin, Y., 2005. U-Pb ages from the neoproterozoic
458 Doushantuo Formation, China. *Science* 308, 95-98.

459 Dahl, T. W., Connelly, J. N., Li, D., Kouchinsky, A., Gill, B. C., Porter, S., Maloof, A. C., Bizzarro, M.,
460 2019. Atmosphere–ocean oxygen and productivity dynamics during early animal radiations. *Proceedings*
461 *of the National Academy of Sciences* 116, 19352-19361.

462 Fike, D.A., Grotzinger, J.P., Pratt, L.M., Summons, R.E., 2006. Oxidation of the Ediacaran ocean. *Nature*
463 444, 744-747.

464 Fike, D. A., Bradley A. S., Rose C. V., 2015 Rethinking the ancient sulfur cycle. *Annual Review of Earth*
465 *and Planetary Sciences* 43, 593-622.

466 Gao, Y., Zhang, X., Zhang G., Chen K., Shen, Y., 2018. Ediacaran negative C-isotopic excursions associated
467 with phosphogenic events: Evidence from South China. *Precambrian Research* 307, 218-228.

468 Grotzinger, J.P., Fike, D.A., Fischer, W.W., 2011. Enigmatic origin of the largest-known carbon isotope
469 excursion in Earth's history. *Nature Geoscience* 4, 285-292.

470 Habicht, K. S. & Canfield, D. E., 1996. Sulphur isotope fractionation in modern microbial mats and the
471 evolution of the sulphur cycle. *Nature* 382, 342-343.

472 He, T., Dal Corso, J., Newton, R.J., Wignall, P.B., Mills, B.J.W., Todaro, S., Di Stefano, P., Turner, E.C.,
473 Jamieson, R.A., Randazzo, V., Rigo, M., Jones, R.E., Dunhill, A.M., 2020. An enormous sulfur isotope
474 excursion indicates marine anoxia during the end-Triassic mass extinction. *Science Advances* 6,
475 eabb6704.

476 Hiess, J., Condon, D. J., McLean N., Noble S. R., 2012 $^{238}\text{U}/^{235}\text{U}$ Systematics in Terrestrial Uranium-Bearing
477 Minerals. *Science* 335, 1610-1614.

478 Knauth, L.P., Kennedy, M.J., 2009. The late Precambrian greening of the Earth. *Nature* 460, 728-732.

479 Lee, C., Love, G.D., Fischer, W.W., Grotzinger, J.P., Halverson, G.P., 2015. Marine organic matter cycling
480 during the Ediacaran Shuram excursion. *Geology*, G37236.37231.

481 Lenton, T. M. & Watson, A. J. Redfield revisited: 1. Regulation of nitrate, phosphate, and oxygen in the
482 ocean. *Global Biogeochemical Cycles* 14, 225-248, (2000).

483 Lenton, T.M., Boyle, R.A., Poulton, S.W., Shields-Zhou, G.A., Butterfield, N.J., 2014. Co-evolution of
484 eukaryotes and ocean oxygenation in the Neoproterozoic era. *Nature Geoscience* 7, 257-265.

485 Li, D., Ling, H., Shields-Zhou, G. A., Chen, X., Cremonese, L., Och, L., Thirlwall, M., Manning, C. J., 2013
486 Carbon and strontium isotope evolution of seawater across the Ediacaran–Cambrian transition: Evidence
487 from the Xiaotan section, NE Yunnan, South China. *Precambrian Research* 225, 128-147,

488 Liu, P. and Moczydłowska. M. 2019. Ediacaran microfossils from the Doushantuo Formation chert nodules
489 in the Yangtze Gorges area, South China, and new biozones in *Fossils and Strata Series* 65, 1-172.

490 Lu, M., Zhu, M., Zhang, J., Shields-Zhou, G., Li, G., Zhao, F., Zhao, X., Zhao, M., 2013. The DOUNCE
491 event at the top of the Ediacaran Doushantuo Formation, South China: Broad stratigraphic occurrence
492 and non-diagenetic origin. *Precambrian Research* 225, 86-109.

493 Maloof, A. C., Porter, S. M., Moore, J. L., Dudás, F. Ö., Bowring, S. A., Higgins, J. A., Fike, D. A., Eddy,
494 M. P., 2010. The earliest Cambrian record of animals and ocean geochemical change. *GSA Bulletin* 122,
495 1731-1774.

496 McFadden, K.A., Huang, J., Chu, X., Jiang, G., Kaufman, A.J., Zhou, C., Yuan, X., Xiao, S., 2008. Pulsed
497 oxidation and biological evolution in the Ediacaran Doushantuo Formation. *Proceedings of the National*
498 *Academy of Sciences* 105, 3197-3202.

499 Rothman, D. H., Hayes, J. M. Summons, R. E., 2003 Dynamics of the Neoproterozoic carbon cycle.
500 *Proceedings of the National Academy of Sciences* 100, 8124-8129,.

501 Sahoo, S.K., Planavsky, N. J., Kendall, B., Wang, X., Shi, X., Scott, C., Anbar, A.D., Lyons, T.W., Jiang,
502 G., 2012. Ocean oxygenation in the wake of the Marinoan glaciation. *Nature* 489, 546.

503 Sawaki, Y., Ohno, T., Tahata, M., Komiya, T., Hirata, T., Maruyama, S., Windley, B. F., Han, J., Shu, D.,
504 Li, Y., 2010. The Ediacaran radiogenic Sr isotope excursion in the Doushantuo Formation in the Three
505 Gorges area, South China. *Precambrian Research* 176, 46-64.

506 Shi, W., Li, C., Luo, G., Huang, J., Algeo, T.J., Jin, C., Zhang, Z., Cheng, M., 2018. Sulfur isotope evidence
507 for transient marine-shelf oxidation during the Ediacaran Shuram Excursion. *Geology* 46, 267-270.

508 Shields, G., Mills, B., Zhu, M., Raub, T., Daines, S., Lenton, T., 2019. Unique Neoproterozoic carbon isotope
509 excursions sustained by coupled evaporite dissolution and pyrite burial. *Nature Geoscience*. 12, 823-827.

510 Stirling, C.H., Andersen, M.B., Potter, E.-K., Halliday, A.N., 2007. Low-temperature isotopic fractionation
511 of uranium. *Earth and Planetary Science Letters* 264, 208-225.

512 Sui, Y., Huang, C., Zhang, R., Wang, Z.,
513 Ogg, J., Kemp, D.B., 2018. Astronomical time scale for the lower Doushantuo Formation of early
514 Ediacaran, South China. *Science Bulletin* 63, 1485-1494.

515 Turner, E.C., Bekker, A., 2016. Thick sulfate evaporite accumulations marking a mid-Neoproterozoic
516 oxygenation event (Ten Stone Formation, Northwest Territories, Canada). *Geological Society of*
517 *America Bulletin* 128, 203–222.

518 Tostevin, R. and Mills, B. J. W., 2020. Reconciling proxy records and models of Earth's oxygenation during
519 the Neoproterozoic and Palaeozoic. *Interface Focus* 10 4 20190137

520 Van Cappellen, P. Ingall, E. D. , 1994. Benthic phosphorus regeneration, net primary production, and ocean
521 anoxia: A model of the coupled marine biogeochemical cycles of carbon and phosphorus.
522 *Paleoceanography* 9, 677-692.

523 Wei, G., Planavsky, N. J., Tarhan, L. G., Chen, X., Wei, W., Li, D., Ling, H., 2018. Marine redox fluctuation
524 as a potential trigger for the Cambrian explosion. *Geology* 46, 587-590.

525 Williams, J.J., Mills, B.J.W., Lenton, T.M., 2019. A tectonically driven Ediacaran oxygenation event. *Nature*
526 *Communications* 10, 2690.

527 Wood, R., Liu, A.G., Bowyer, F., Wilby, P.R., Dunn, F.S., Kenchington, C.G., Cuthill, J.F.H., Mitchell, E.G.,
528 Penny, A., 2019. Integrated records of environmental change and evolution challenge the Cambrian
529 Explosion. *Nature Ecology and Evolution* 3, 528-538.

530 Wortmann, U.G., Paytan, A., 2012. Rapid Variability of Seawater Chemistry Over the Past 130 Million Years.
531 *Science* 337, 334-336.

532 Xiao, S., Zhang, Y., Knoll, A.H., 1998. Three-dimensional preservation of algae and animal embryos in a
533 Neoproterozoic phosphorite. *Nature* 391, 553.

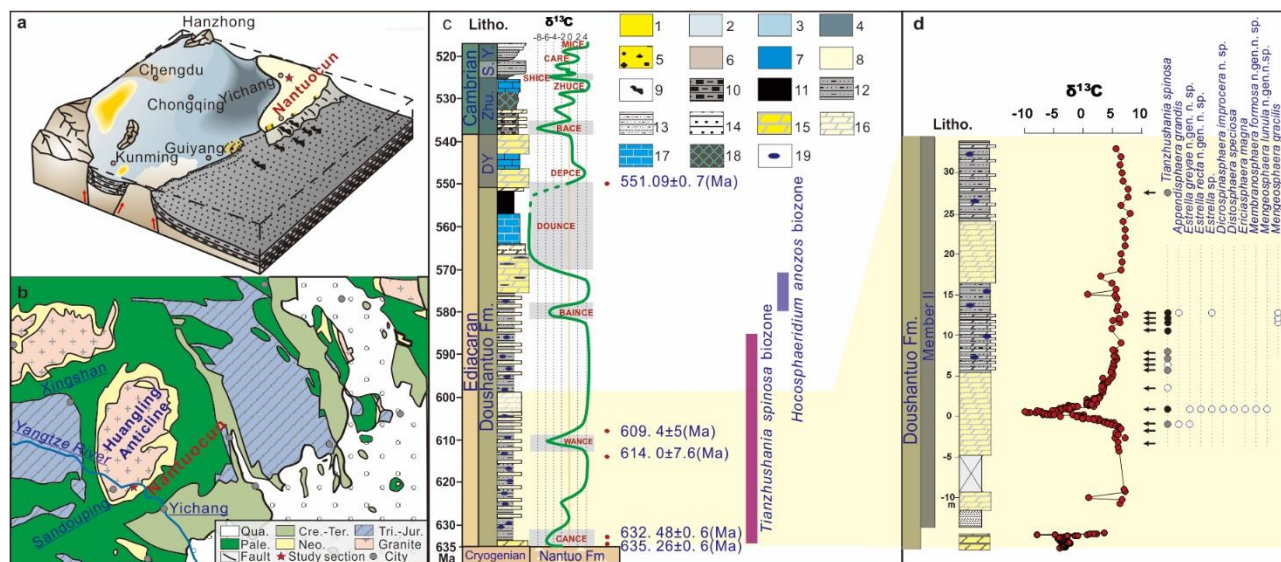
534 Yuan, X., Chen, Z., Xiao, S., Zhou, C., Hua, H., 2011. An early Ediacaran assemblage of macroscopic and
535 morphologically differentiated eukaryotes. *Nature* 470, 390.

536 Zhang, F., Romaniello, S. J., Algeo, T. J., Lau, K. V., Clapham, M. E., Richoz, S., Herrmann, A. D., Smith,
537 H., Horacek, M., Anbar, A. D., 2018. Multiple episodes of extensive marine anoxia linked to global
538 warming and continental weathering following the latest Permian mass extinction. *Science advances* 4,
539 e1602921,.

540 Zhang, F., Xiao, S., Romaniello, S. J., Hardisty, D., Li, C., Melezhik, V., Pokrovsky, B., Cheng, M., Shi,
541 W.,Lenton, T. M.,Anbar, A. D., 2019. Global marine redox changes drove the rise and fall of the Ediacara
542 biota. *Geobiology* 17, 594-610,

543 Zhou, C., Yuan, X., Xiao, S., Chen, Z., Hua, H., 2018. Ediacaran integrative stratigraphy and timescale of
544 China. *Science China Earth Sciences* 62, 7-24.

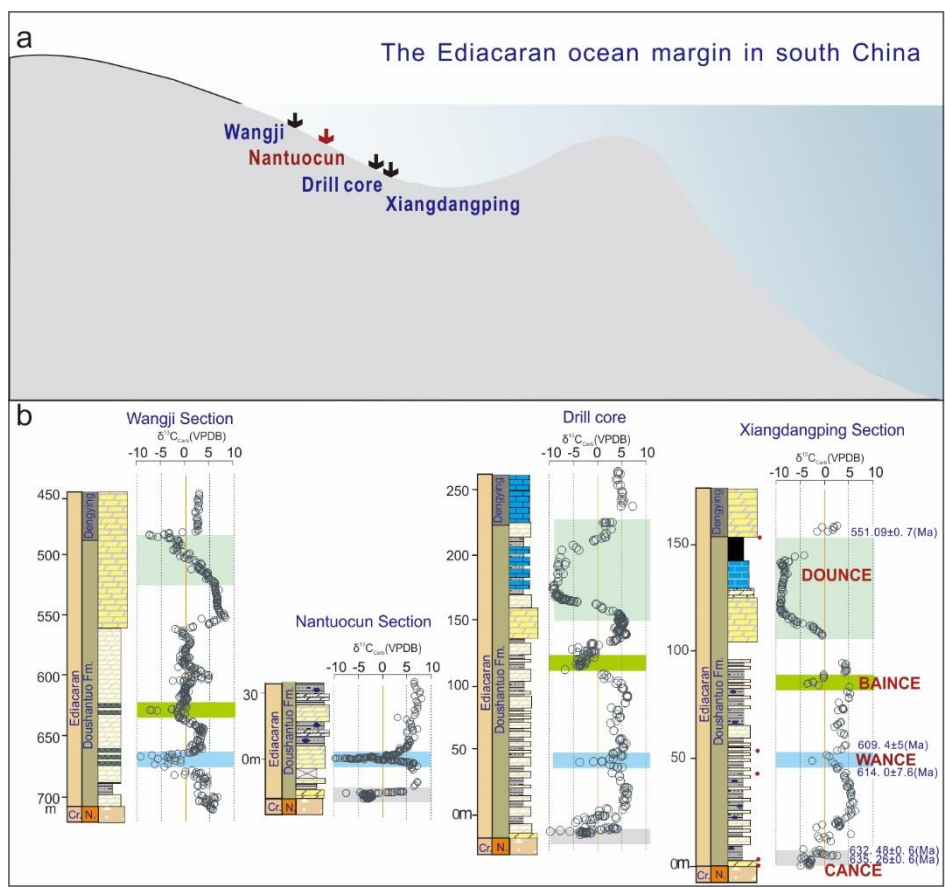
544 Zhou, C., Li, X., Xiao, S., Lan, Z., Ouyang, Q., Guan, C., Chen, Z., 2017. A new SIMS zircon U–Pb date
 545 from the Ediacaran Doushantuo Formation: age constraint on the Weng'an biota. Geological Magazine
 546 154, 1193-1201
 547 Zhu, M., Zhang, J., Yang, A., 2007. Integrated Ediacaran (Sinian) chronostratigraphy of South China.
 548 Palaeogeography, Palaeoclimatology, Palaeoecology 254, 7-61.
 549 Zhu, M., Lu, M., Zhang, J., Zhao, F., Li, G., Yang, A., Zhao, X., Zhao, M., 2013. Carbon isotope
 550 chemostratigraphy and sedimentary facies evolution of the Ediacaran Doushantuo Formation in western
 551 Hubei, South China. Precambrian Research 225, 7-28.
 552
 553
 554
 555
 556
 557
 558
 559
 560
 561



562
 563
 564 **Fig. 1 Geological setting and stratigraphy of the Nantuocun section, Yichang, western**
 565 **Hubei, South China.** a. Paleogeographical and b. geological map showing the location of the
 566 Nantuocun Section. Qua. = Quaternary, Cre. -Ter. = Cretaceous-Tertiary, Tri. -Jur. = Triassic-
 567 Jurassic, Pale. = Paleozoic, Neo. = Neoproterozoic. CANCE = Cap carbonate Negative Carbon
 568 isotope Excursion, WANCE = Weng'An Negative Carbon isotope Excursion, BAINCE=
 569 Baiguoyuan Negative Carbon isotope Excursion, DOUNCE = Doushantuo Negative Carbon
 570 isotope Excursion. DEPCE = Dengying Positive Carbon isotope Excursion, BACE = Basal
 571 Cambrian Carbon isotope Excursion ZHUCE = Zhujiaying Carbon isotope Excursion, SHICE=
 572 Shiyantou Carbon isotope Excursion CARC= Cambrian Arthropod Radiation isotope
 573 Excursion, MICE = Mingxinsi Carbon Isotope Excursion, c. The generalized litho- and $\delta^{13}\text{C}_{\text{carb}}$
 574 stratigraphy of the Ediacaran and early Cambrian of the South China (Zhu et al., 2013), and

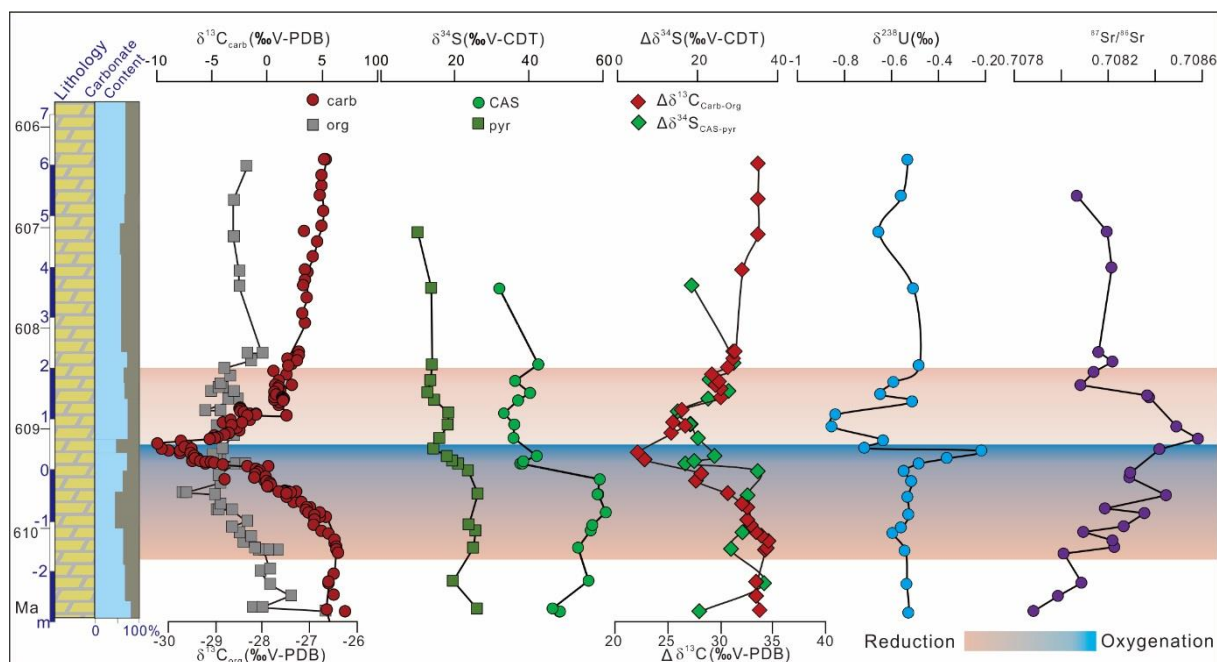
575 available radiometric and biostratigraphic data for the Doushantuo Formation (Condon et al.,
 576 2005; Zhou et al., 2017) DY = Dengying, Zhu. = Zhujiaying, S. = Shiyantou, Y. = Yuanshan,
 577 FM. = Formation. d. Litho-, bio- and $\delta^{13}\text{C}_{\text{carb}}$ stratigraphy of the Nantuocun section. Yellow
 578 shadow showing stratigraphic correlation of the Nantuocun section within the Doushantuo
 579 Formation. Legends for c and d: 1. Inter-carbonate platform restricted basin; 2. Coarse clastic
 580 basin; 3. Fine clastic basin; 4. Deep water silt and shales basin; 5. Shoal in carbonate platform;
 581 6. Landmass; 7. Inter-carbonate platform deep water basin; 8. Carbonate platform; 9. Slumps;
 582 10. Siliceous rock; 11. Black shale; 12. Black silty shale; 13. Silty shale; 14. Sandstone; 15.
 583 Cap carbonate; 16. Dolostone; 17. Limestone; 18. Phosphorite; 19. Cherty concretions.

584
 585
 586
 587
 588

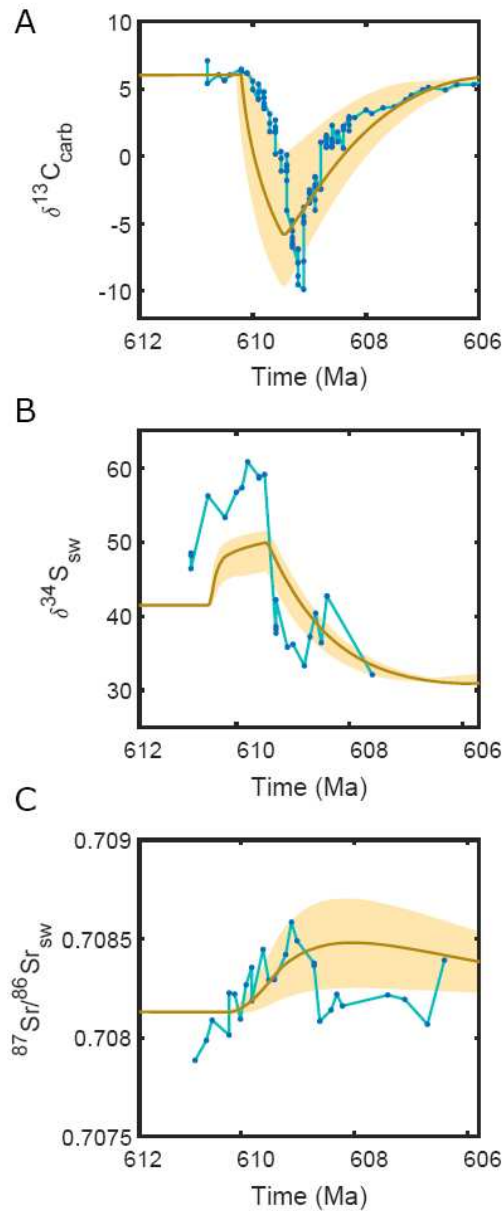


589
 590 **Fig. 2 Palaeogeographic reconstruction of the shelf-to-basin transect showing the wide**
 591 **occurrence of WANCE in the Yangtze Gorges area. Legends in b see Fig. 1 data for**

592 Xidangdangping section from Zhu et al. (2013), Drill cole Sawaki et al. (2010), Wangji section
 593 Gao et al. (2018).
 594
 595
 596

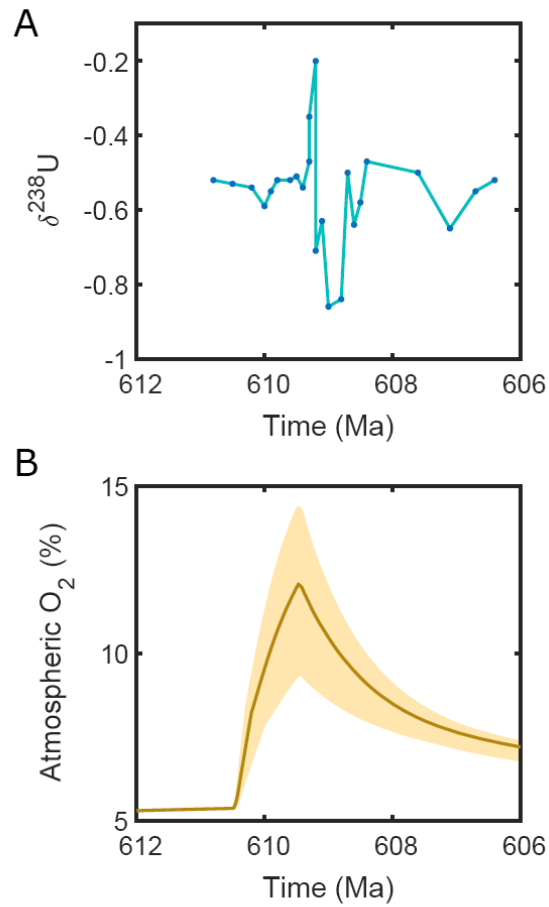


597
 598 **Fig. 3 Paired profiles of inorganic ($\delta^{13}\text{C}_{\text{carb}}$) and organic carbon ($\delta^{13}\text{C}_{\text{org}}$), and pyrite**
 599 **($\delta^{34}\text{S}_{\text{pyr}}$) and carbonate associated sulfate ($\delta^{34}\text{S}_{\text{CAS}}$) isotopes, and $\Delta^{13}\text{C}_{\text{carb}}$, $\Delta^{34}\text{S}$, $\delta^{238}\text{U}$**
 600 **and $^{87}\text{Sr}/^{86}\text{Sr}$ records for the early Ediacaran WANCE event at the Nantuocun section,**
 601 **South China.** See Supplementary Information for stratigraphic details. Carbon and sulfur
 602 isotope data are reported relative to Vienna Pee Dee Belemnite (VPDB) and Vienna Cañon
 603 Diablo Troilite (VCDT), respectively. $\Delta^{13}\text{C} = \delta^{13}\text{C}_{\text{carb}} - \delta^{13}\text{C}_{\text{org}}$ and $\Delta^{34}\text{S} = \delta^{34}\text{S}_{\text{CAS}} - \delta^{34}\text{S}_{\text{pyr}}$.
 604 $\delta^{238}\text{U}$ is reported relative to the NBL CRM-145 natural U standard.
 605



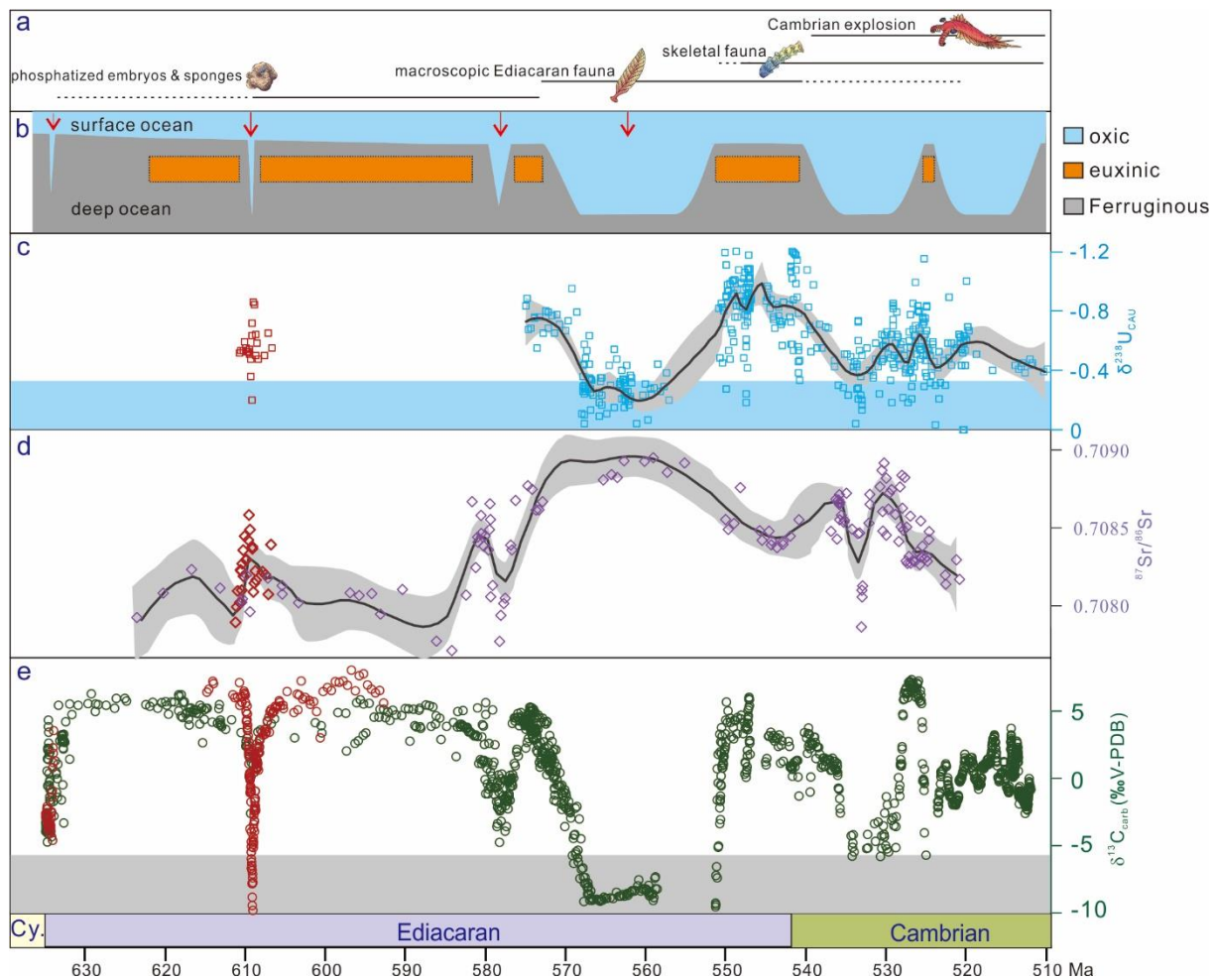
606
607

608 **Fig. 4. COPSE model output against measured isotope ratios.** The most recent COPSE
609 model version (Tostevin and Mills, 2020) is run through the Ediacaran period, with the
610 inclusion of a large reservoir of DOM, following the model approach in Shields et al. (2019).
611 The model is subjected to a stepwise increase in gypsum-derived sulfate input from weathering
612 between 610.5 Ma and 609.5 Ma. The input of pyrite-derived sulfate is also increased at the
613 same time, but remains elevated throughout the model run, reflecting the different weathering
614 dynamics. A. $\delta^{13}\text{C}_{\text{carb}}$ of marine carbonate. B. $\delta^{34}\text{S}_{\text{sw}}$ of seawater sulfate. C. $^{87}\text{Sr}/^{86}\text{Sr}_{\text{sw}}$ of seawater.
615 Yellow shading shows model output under 5-15 fold enhancements in gypsum weathering, with
616 the central line showing a 10-fold enhancement. Blue dots show measured datapoints.



617
618
619

620 **Fig. 5. COPSE model output for oxygenation.** A. $\delta^{238}\text{U}$ values reported as a function of time.
621 B. Model outputs for the size of the combined atmosphere-ocean O_2 reservoir. Yellow shading
622 shows model output under 5-15 fold enhancements in gypsum weathering, with the central line
623 showing a 10-fold enhancement. Blue dots show measured datapoints.



624
 625
 626
 627
 628
 629
 630
 631
 632
 633
 634
 635
 636
 637
 638

Fig. 6. Integrated key metazoan innovations and ocean oxygenation patterns, and their correlation to marine uranium, strontium and carbon isotopic records, for the Ediacaran and early Cambrian Period. a. The timeline of key evolutionary innovations for metazoans. b. Oxygenation pattern for the Ediacaran and early Cambrian oceans based on this study. c. Uranium isotope record (red squares, this study; blue squares from (Zhang et al., 2018; 2019; Wei et al., 2018; Dahl et al., 2019) and blue shading represent the values above the modern ocean. d. Strontium isotope record (red diamonds, this study; dark blue diamonds from (Sawaki 2010; Maloof, et al., 2010; Li et al., 2013). e. Carbon isotope record (red circles, this study; green circles from (Lu et al., 2013; He et al., 2019; Li et al., 2013) for the Ediacaran and early Cambrian, grey shading represents values below that of mantle input. Black lines with grey shading in (c) and (d) represent a Locfit regression with 95% confidence interval.

639

640 **Acknowledgements** This work was supported by the Strategic Priority Research Program (B)
641 of the Chinese Academy of Sciences (XDB18000000) and National Natural Science
642 Foundation of China (41661134048) to M.Z., NERC (NE/S009663/1) to B.J.W.M. and S.W.P.,
643 the NERC-NSFC programme ‘Biosphere Evolution, Transitions and Resilience’ through grant
644 NE/P013643/1 to G.A.S. and S.W.P., NERC (N018559/1) to R.J.N. and S.W.P., and the State
645 Key Laboratory of Palaeobiology and Stratigraphy, Chinese Academy of Sciences (No.
646 20172101; No.2018KF03) to B. C. and T.H., S.W.P. additionally acknowledges support from
647 a Royal Society Wolfson Research Merit Award. We acknowledge Tian Chao for assistance
648 with figure preparation and Li Guang and S. Reid for assistance in the field work and
649 geochemical analyses.

650